Article

Terahertz Scanning Tunneling Microscopy for Visualizing Ultrafast Electron Motion in Nanoscale Potential Variations

Shoji Yoshida, Yusuke Arashida, Hideki Hirori, Takehiro Tachizaki, Atsushi Taninaka, Hiroki Ueno, Osamu Takeuchi, and Hidemi Shigekawa*

Cite This: *ACS Photonics* 2021, 8, 315−323

Read Online

ACCESS | Metrics & More | Article Recommendations | Supporting Information

ABSTRACT: Studying the microscopic behavior of free carriers in materials at an ultrashort time scale is critical to developing semiconductor, optoelectronic, and other technologies satisfying the ever-increasing requirements for smaller sizes and higher speeds. Understanding the effect of local potential modulations and localized states due to nanoscale microstructures on carrier dynamics is essential to realize these requirements. Here, we used time-resolved scanning tunneling microscopy/spectroscopy (STM/STS) combined with a carrier-envelope phase (CEP)-controlled subcycle THz electric field, THz-STM, to probe the ultrafast motion of electrons photoinjected into C_{60} multilayer structures grown on Au substrate. We have succeeded in demonstrating the time-resolved measurement of ultrafast electron dynamics with sub-nanoscale spatial resolution and subcycle time

Nanoscale snapshots of ultrafast electron motion

resolution for the first time and successfully visualized the electron motion triggered by the spatial variation in the lowest unoccupied molecular orbital (LUMO). The difference in the effects of molecular defects, such as a molecular vacancy and orientational disorder, was also clearly distinguished with single-molecular-level spatial resolution. This method is expected to play an important role in the precise evaluation of local electronic structures and dynamics for the future development of new functional materials and device elements.

KEYWORDS: *ultrafast electron dynamics, scanning tunneling microscopy, terahertz, organic film, C_{60}, time-resolved imaging*

In the development of functional materials and devices, atomic-scale structures such as defects, steps, and impurities have large effects on carrier (electron and/or holes) dynamics because of their local potential modulations and localized electronic states.[1] Therefore, understanding how nanoscale structural disorders in materials affect the dynamics of free carriers has been an essential issue, for example, in semiconductor physics, optoelectronics, and photochemistry. In particular, visualization of phenomena such as ultrafast electron motion in a nanoscale potential variation and the dynamics of charge transfer between molecules with a high spatiotemporal resolution has been challenging.[2] The methods of imparting high time resolution to scanning tunneling microscopy (STM) have high potential for such purposes. Among the microscopy techniques, optical pump−probe (OPP) STM, which combines optical technologies and STM, is effective.[3−5] Recently, terahertz (THz)-STM, a measuring method of using a subcycle pulse electric field in the THz region as an applied voltage, has been developed and has been attracting attention.[6−8] In OPP-STM, a high spatiotemporal resolution was realized, which allows us to probe various physical phenomena on their intrinsic time and space scales. However, the visualization of the ultrafast dynamics of electron motion
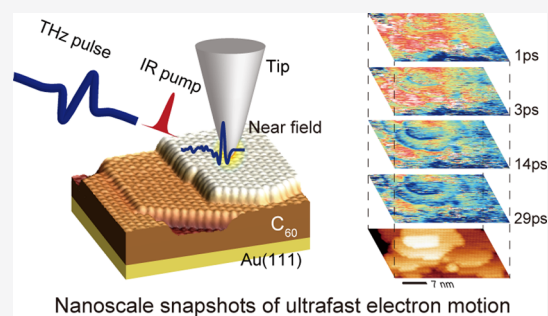
and charge transfer has not yet been realized using these methods.

In this study, we used THz-STM to probe the ultrafast dynamics of free electrons photoinjected into a C_{60} multilayer film formed on a Au(111) substrate. Research on the ultrafast dynamics of photoexcited carriers in a C_{60} multilayer film has been actively pursued from the perspective of optoelectronic device applications such as solar cells and field effect transistors (FETs).[9−11] Since a C_{60} thin film is formed by the weak van der Waals interaction between molecules, as is common for general organic thin films, charge transport occurs owing to the hopping of electrons between molecular orbitals in neighbor sites. Consequently, a change in the molecular interaction owing to structural disorder will strongly affect the motion of electrons. Thus, the molecular-scale measurement of electron dynamics will provide insight into the charge transport in organic materials. By measuring the spatiotemporal variation of
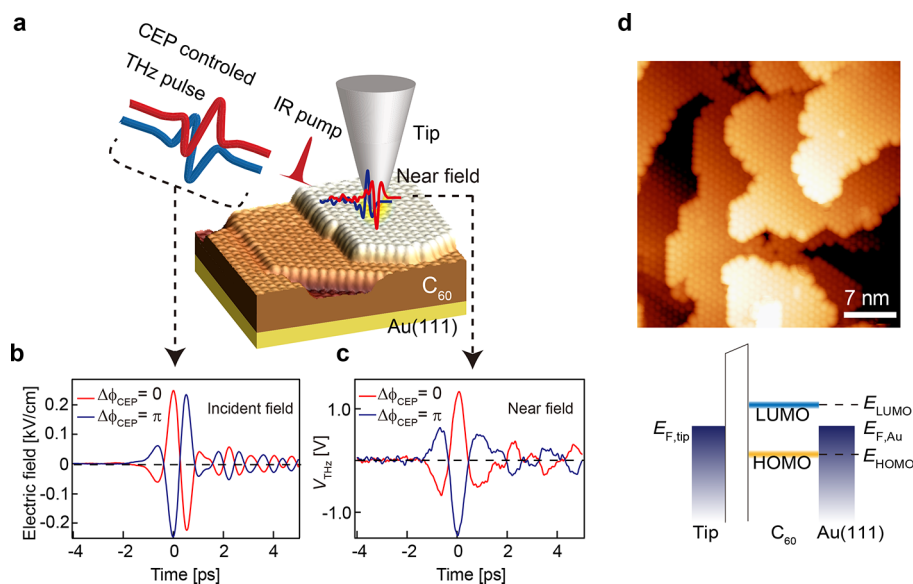
Figure 1. Measurement system and sample. (a) Schematic illustration of the measurement setup. (b) Waveform of incident electric field for $\Delta\Phi_{CEP}$ = 0 and π. (c) Waveform of near-field electric field for $\Delta\Phi_{CEP}$ = 0 and π. (d) STM image of the sample. (e) Band diagram of the STM tunnel junction at equilibrium ($E_{LUMO} - E_{F,Au}$ = 0.9 eV, $E_{F,Au} - E_{HOMO}$ = 2.2 eV).

THz-induced tunnel current (I_{THz}), we have succeeded in visualizing electron motion in real space for the first time at a sub-nanoscale spatial resolution under the influence of the nanoscale potential modulation.

■ RESULTS AND DISCUSSION

Measurement Setup and Sample Preparation. Figure 1 shows a schematic of the measurement setup (see Materials and Methods and Figure S1 for details). In THz-STM, an IR pulse (1035 nm, 309 fs width) was used as the pump to excite the sample, and a carrier envelope phase (CEP)-controlled single-cycle THz pulse was used as the probe. Figure 1b shows the incident THz electric field waveform measured by electro-optical (EO) sampling, and Figure 1c shows the THz near-field waveform at the probe tip measured by the photoemission technique (see Figure S2 for details). The CEP can be controlled between 0 and π using a THz-CEP shifter (see Figure S1).[8,12,13] The voltage $V_{THz-Peak}$ produced at the maximum point of the THz near field used here was 1.5 V (see Figure S3). Figure 1d shows a typical STM image of the sample. Figure 1e shows the band diagram of the tunnel junction at the equilibrium condition. The energy position of the lowest unoccupied molecular orbital (LUMO) of C_{60} (E_{LUMO}) is 0.9 eV above the Fermi energy of Au(111) ($E_{F,Au}$), and that of the highest occupied molecular orbital (HOMO) of C_{60} (E_{HOMO}) is 2.2 eV below $E_{F,Au}$.

Relationship between THz Current and Electron Dynamics. When an infrared (IR) pump pulse is irradiated to the C_{60} multilayer film sample, hot electrons excited in the Au(111) surface are injected into the C_{60} LUMO, as shown in Figure 2a (II). The accumulation of electrons in the sample's outermost surface reduces and flattens the tip-induced band bending (TIBB), similarly to the surface photovoltage (SPV) mechanism.[14,15] After that, the LUMO electrons return to their original state by diffusion to the Au(111) substrate, during which the electrons move around and their distribution in the LUMO simultaneously changes, but some electron tunneling to the tip side is detected by THz-STM, enabling us to observe the dynamics induced by IR laser pulse irradiation.
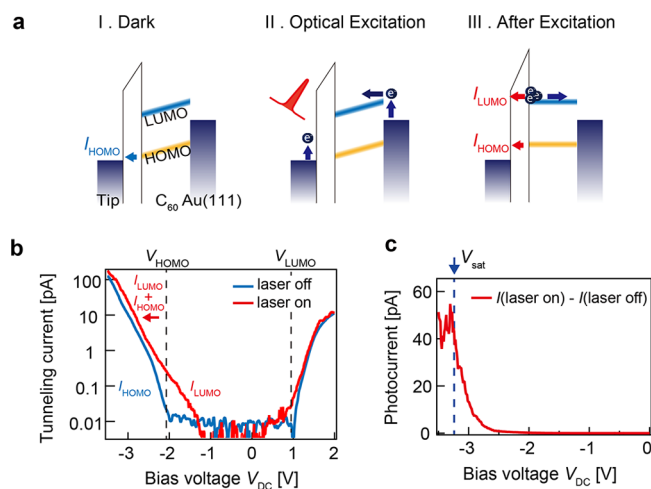
Figure 2. IR-laser-pulse-induced change in the tunneling junction. (a) Change in the band diagram of a tunnel junction with IR pulse irradiation. (b) $I-V$ curves with (red) and without (blue) IR irradiation. The THz pulse was blocked and the IR pulse irradiation was turned on and off during the measurement (set point V_{DC} = +2.0 V, I_t = 10 pA). V_{DC} represents the DC bias voltage applied to the sample. I_{HOMO} and I_{LUMO} are the tunnel currents from the HOMO and LUMO states, respectively. At a high negative bias voltage ($V < V_{HOMO}$) where I_{HOMO} appears, the tunnel current becomes the sum of I_{LUMO} and I_{HOMO}. (c) V_{DC} dependence of the photocurrent obtained by subtracting the $I-V$ curve in the IR-off state from that in the IR-on state.

To see the above-described process, we first compared the tunnel current-bias voltage ($I-V$) curves measured with and without IR pulse excitation (Figure 2b). Here, only DC bias voltage V_{DC} was applied. The THz pulse was blocked and the IR pulse irradiation was turned on and off during the measurement. In the laser-off (IR-off) state, tunneling from the HOMO (= I_{HOMO}) to the tip determines the shape of the $I-V$ curve for a negative bias voltage, including TIBB, as shown in Figure 2a (I). On the other hand, in the laser-on (IR-on) state, in addition to I_{HOMO}, which is shifted by SPV as
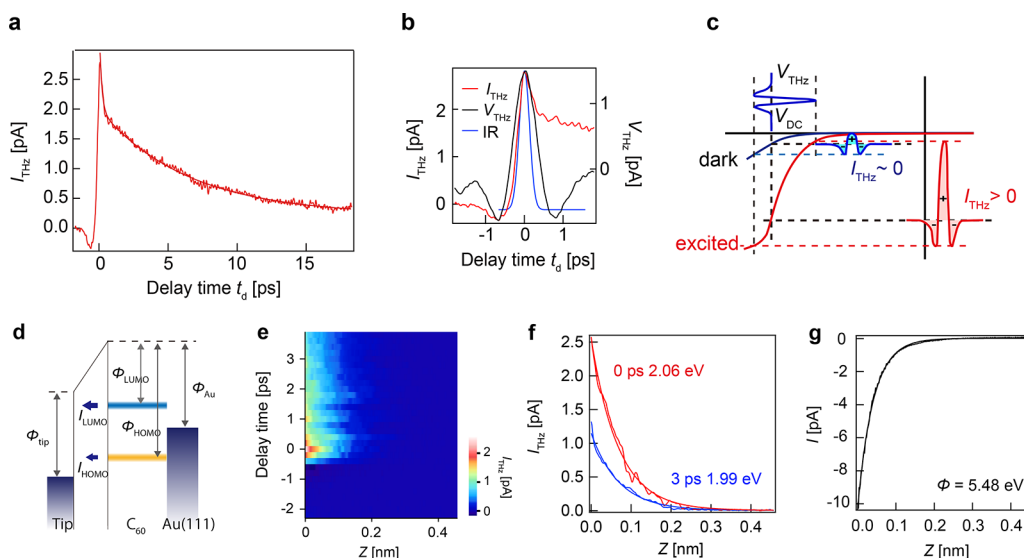
Figure 3. Analysis of the THz-STM signal. (a) Delay time dependence of THz current after IR-pulse excitation ($\Delta\Phi_{CEP} = 0$, $V_{DC} = -3.0$ V, $I_t = 10$ pA, IR: 20 mW). (b) An enlargement of the initial change in (a). The blue and black curves show a Gaussian pulse with a width of 309 fs showing the IR pulse and the THz waveform, respectively. (c) Schematic model showing the relationship between the waveform of the bias voltage $V_{THz}(t)$ applied to the STM tunnel junction by the THz pulse ($\Delta\Phi_{CEP} = 0$) and the shape of the THz-induced current $I_{THz}(t)$ obtained for the $I-V$ curves of the IR-on (red) and IR-off (blue) states, which correspond to those in Figure 2b, at delay time $t = t_d$. (d) Band diagram of tunnel junction at tunnel voltage of $V_S = -3.0$ V. (e) Delay time dependence of $I_{THz}-z$ curve ($\Delta\Phi_{CEP} = 0$, $V_{DC} = -3.0$ V, $I_t = 10$ pA, IR: 20 mW). (f) $I_{THz}-z$ curves obtained at 0 and 3 ps and exponential fitting. (g) $I_{DC}-z$ curve measured under the same conditions as in (f).

shown in Figure 2a (III), an increase due to the electron tunneling from the LUMO (= I_{LUMO}) is expected. In fact, the photocurrent from the sample to the tip was observed from a voltage much lower than the energy position of the HOMO (V_{HOMO}), as shown in Figure 2b, which is considered to reflect the electron tunneling from the LUMO to the probe tip.

Figure 2c shows the bias voltage dependence of the photocurrent obtained by subtracting the $I-V$ curve of the IR-off state from that of the IR-on state. I_{LUMO} is expected to increase with the bias voltage due to the reduction of the effective tunnel barrier height shown in Figure 2a (III). However, experimentally, saturation of the photocurrent was observed for a negative bias voltage higher than V_{sat}, as shown in Figure 2c. This is because the number of electrons excited into the LUMO by each IR pulse was finite, which is considered to limit the number of electrons tunneling from the LUMO to the probe tip during the measurement time.

Next, we carried out IR-pump and THz-probe measurements to observe the photoinjected electron dynamics in the C_{60} multilayer. A THz pulse was applied in addition to V_{DC}, modulating the bias voltage. We used the lock-in measurement method by chopping the THz laser pulses at a frequency of 415 Hz. Figure 3a shows a typical time-dependent THz-STM signal $I_{THz}(t_d)$ after IR excitation. We observed an abrupt increase in $I_{THz}(t_d)$ at $t_d = 0$, followed by exponential decay with time ($t_d > 0$), thus showing the time-resolved signal.

Regarding the fast component, Figure 3b shows a magnified view of the region near 0 ps in Figure 3a, where the IR pulse (309 fs pulse width) and THz pulse are shown superimposed on the initial peak. The apparent signal shows the decay at the similar width as that of the THz pulse. The result shows that there exists a signal faster than the change in the temporal resolution of the system. Namely, this signal was widened during the measurement owing to the convolution with IR and THz pulses. Therefore, the original signal is considered to have a shorter lifetime. In fact, the dip present around $t_d = -0.8$ ps is

considered to indicate that the THz pulse waveform was probed by this fast signal, which is similar to the process performed in the previous study using the fast relaxing electrons in Bi_2Se_3.[8] The time scale of the fast decay is comparable to the cooling time of hot electrons photoexcited in a metal tip (about 100 fs)[16] and those excited into higher LUMO levels in a molecular multilayer (about 50 fs).[9] Since time-resolved measurements using a shorter pulse system are necessary to obtain more details,[17−19] we leave this issue for future investigation and do not pursue this phenomenon in detail in this paper.

In THz-STM, instead of a rectangular pulse voltage, a time-dependent voltage $V_{THz}(t)$ whose waveform corresponds to that of the THz electric field is applied. Therefore, $I_{THz}(t_d)$ is defined here as

$$I_{THz}(V_{DC}, t_d) = f_{rep} \int_{t_d}^{t_d + 1/f_{rep}} [I\{V_{DC} + V_{THz}(t)\} - I(V_{DC})] dt \tag{1}$$

where f_{rep} is the repetition frequency of the IR and THz lasers. Because $I_{THz}(t)$ depends on the nonlinearity of the $I-V$ curve, $I_{THz}(t)$ also depends on V_{DC}. We used the schematic model shown in Figure 3c where two $I-V$ curves corresponding to those in Figure 2b are drawn for the analysis. The relationship between the waveform of the bias voltage $V_{THz}(t)$ applied to the STM tunnel junction by the THz pulse and the shape of the THz-induced current $I_{THz}(t)$ obtained for the $I-V$ curves of the IR-on (red) and IR-off (blue) states at the delay time $t = t_d$ is shown. A negative V_{DC} was applied to the sample to inject electrons from the Au substrate into the LUMO of the sample by IR irradiation. When we applied a THz pulse, the transient voltage $V_{THz}(t)$ produced by the THz electric field modulated the tunnel bias voltage V_{DC}, producing the transient THz current $I_{THz}(t)$ at each delay time t_d, as shown in Figure 3a. Since it has become possible to experimentally obtain the near-

field waveform immediately below the probe tip,[8] such analysis has become possible.

For $\Phi = 0$ ($V_{THz} > 0$), as $V_{THz,peak}$ increases, the tunneling probability decreases, reducing the tunnel current. However, if the temporal change in electron density in LUMO is slower than that of the THz pulse, that is, if the electron density is assumed to be constant during the period when the THz field is changing, $I_{THz}(t_d)$ obtained using eq 1 is considered to be almost proportional to the electron density for $t = t_d$. Therefore, THz-STM can be effectively used when $\Phi = 0$, and the effects of electron extraction and the tunnel current from HOMO are not apparent. For $\Phi = \pi$ ($V_{THz} < 0$), however, if the number of electrons is limited, as in the sample used in this experiment, the effect of electron extraction may appear as shown in Figure 2c, which complicates the analysis of $I_{THz}(t_d)$. Leaving detailed analysis for future work, all the following experiments were performed with the THz pulse of $\Phi = 0$.

Next, we performed $I_{THz}-z$ measurement to investigate the dominant tunnel channel (I_{HOMO} or I_{LUMO}) in I_{THz}. I_{HOMO} or I_{LUMO} can be distinguished by $I_{THz}-z$ measurement because I_{HOMO} and I_{LUMO} have their own effective vacuum barrier heights, as shown in Figure 3d. Their apparent barrier heights Φ can be obtained from the decay constant κ of the tunnel current expressed as

$$I(z) \propto \exp(-2\kappa z) \quad \kappa = \sqrt{2m\phi/\hbar} \tag{2}$$

where m is the electron mass and $\hbar$ is the Dirac constant. Figure 3e shows the delay time dependence of the $I_{THz}-z$ curve, and Figure 3f shows the $I_{THz}-z$ curves obtained for $t_d = 0$ and 3 ps. The values of Φ obtained by exponential fitting were 2.06 eV at $t_d = 0$ ps and 1.99 eV at $t_d = 3$ ps. The barrier height measured from the $I_{DC}-z$ curve shown in Figure 3g was 5.48 eV.

The work function of the W tip, Φ_{tip}, and that of the Au(111) substrate, Φ_{Au}, are 4.5 and 4.74 eV, respectively. Since the LUMO and HOMO levels are 0.9 and −2.2 eV with respect to the Au Fermi surface,[20] Φ_{LUMO} and Φ_{HOMO} in Figure 3d become 3.64 and 6.94 eV, respectively. Since $V_{DC} = -3.0$ V in the experiment, the barrier height for I_{HOMO} becomes 5.32 eV. This is in good agreement with the value obtained from the $I_{DC}-z$ curve shown in Figure 3g. Similarly, the barrier for the electrons in I_{LUMO} was obtained to be 2.22 eV, which is also in good agreement with the value obtained from the $I_{THz}-z$ curve shown in Figure 3f. The results demonstrate the dominant contribution of I_{LUMO} to I_{THz}, as expected. The fast component in Figure 3a is not observed here. Since the modulation by V_{THz} is not included in the above consideration, this is not a strict treatment, but it is considered sufficiently rigorous for a qualitative evaluation. If the signal was stronger and the measurement with a longer delay time than those in Figure 3f was possible, TIBB would have been reproduced.

In the actual measurement, the electron extraction may affect the decay process. Therefore, we investigated the set point current dependence of the time-resolved spectrum (Figure 4a), and the result is summarized in Figure 4b. When the set point current was increased by one order and the tip was moved closer, the lifetime was reduced by about 10%. Although an effect of the set point current dependence existed, it can be reduced by selecting appropriate measurement conditions. When the set current I_t was decreased to 2 pA, the fast component disappeared. This is considered to correspond
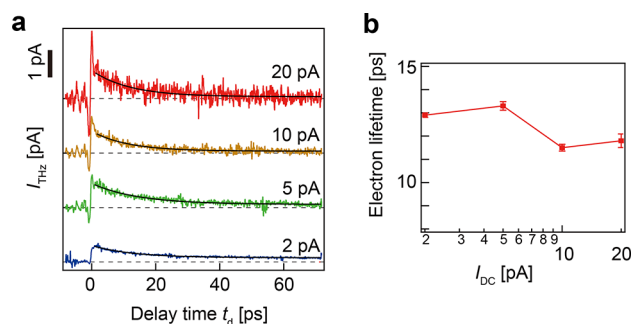
Figure 4. Effect of electron extraction. (a) Delay time dependence of the THz current at different set point currents I_{DC} ($\Delta\Phi_{CEP} = 0$, $V_{DC} = -3.0$ V, IR: 20 mW). (b) Set point current dependence of the lifetime shown in (a).

to the observation that no fast component appeared in Figure 3f. These results suggest that the probability of tunneling the fast component in the short time may not be sufficient at this distance. The discussion on this issue is beyond the scope of this paper, a more detailed analysis is left for future work.

We carried out the experiments under the conditions discussed here. Thus, the signal observed for $t_d > 0$ in Figure 3a represents the photoinjected electron population in the LUMO state below the STM tip. An electron lifetime of 6.4 ps was obtained by fitting using an exponential function. Compared with the interlayer hopping rate (3×10^{13} s^{-1}) obtained using time-resolved two-photon photoemission,[21] our measured electron lifetime is long. This difference is considered to be caused by the negative sample bias voltage applied in the experiments, as shown by the band diagram in Figure 2a.

Imaging Electron Motion with Sub-nanoscale Resolution. Next, we measured the spatial variation of $I_{THz}(t_d)$ to analyze the motion of electrons injected into the LUMO, which is the first ever visualization of the spatial motion of electrons with sub-nanoscale resolution. Figure 5a shows an STM image of the C_{60} multilayer structure in a region including steps and terraces, and Figure 5b shows the time-resolved spectra obtained at different points in the STM image. The spectra were simply fitted with the sum of three components,

$$I(t_d) = -A\exp(-t_d/\tau_r) + B\exp(-t_d/\tau_d) + C \tag{3}$$

where τ_r, τ_d, t_d, and C represent the lifetimes of the initial increase and the subsequent decay components, the delay time, and a constant term due to a lifetime longer than the system limitation, respectively. As shown by the solid black lines on the spectra, the agreement was good, and the values of τ_r and τ_d are shown to the right of the figure. τ_r is considered to represent a process in which electrons accumulate immediately below the probe tip after electron injection, and τ_d represents a process in which electrons return to the Au substrate.

The features of the signals are as follows.

1. The top layer (A to C) has no initially rising component.
2. From the second layer, the lifetime of the initial increase in τ_r (0.3 to 1.5 ps) is nonzero except at the upper step edge (D).
3. The lifetime of the decay τ_d has a relatively large value near the vacancy defect indicated by the arrow and around the down step edge.
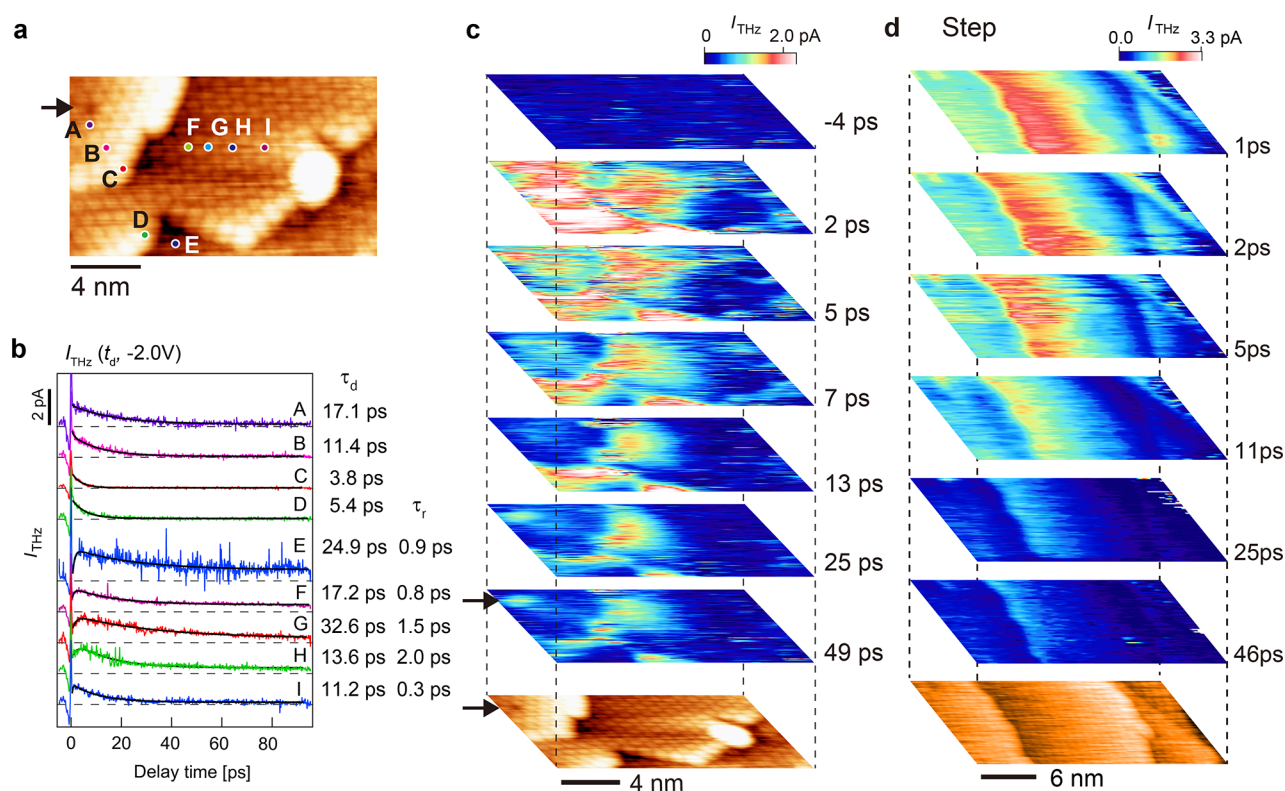
Figure 5. Time-resolved analysis of electron motion for steps and a vacancy defect. (a) STM image of the C_{60} multilayer structure in a region including steps and a vacancy defect, indicated by the arrow. (b) Time-resolved spectra obtained at A to I in (a). I_{THz} represents the THz-induced current. See Materials and Methods for details of the fitting. (c) Snapshots obtained over the area shown in (a). (d) Snapshots obtained over a wider area including steps. $(V_{DC}, I_t) = (-2.0 \text{ V}, 10 \text{ pA})$.

4. From the second layer, except at the upper step edge (D) and around the white cluster in the middle right (I), the constant term C in eq 3 (a long-lifetime component considered to be in the sub-ns to ns range) is nonzero. Although our system cannot measure this long lifetime because of the limited length of the optical delay line ($<\sim$300 ps), the condition returned to the initial state when the next IR pulse was irradiated.

To visualize the electron dynamics in more detail, 2D imaging of the THz current was performed, as shown in Figure 5c. The snapshots were obtained by repeatedly scanning over the same area while changing the delay time from -4 to 49 ps. At -4 ps, the THz current was almost zero, indicating that the THz current was observed only under excitation by the IR pulse. At 2 ps after IR pulse irradiation, the electron density was widely distributed except around the white cluster on the right-side step. The electron density rapidly decreased in the top layer, whereas electrons accumulated near the down step area and around the defect indicated by the arrow and remained even after 49 ps. By assembling these I_{THz} images taken at different delay times, we made a movie that directly shows the nanoscale motion of electrons in the ps time scale (see Supplementary Movie S1). The characteristics of each spectrum were clearly observed. The electron dynamics around a step are shown more clearly in Figure 5d, which was obtained by a wider-area scan.

Regarding the component that rises at the initial stage, the lifetime was obtained by fitting the spectra in Figure 5b (E−I). Although the lifetime of 0.3 ps is comparable to the resolution of the system, a signal exists because its shape is different from those of the spectra A to D in Figure 5b. Since the horizontal

diffusion was fast and the distribution of injected electrons was already formed at $t_d = 1$ ps, the initial horizontal change in the red area with high electron density is not very clear in the snapshots. However, a gradual decrease in the high-density area can be seen in the images in Figures 5a and 5b, showing the existence of the horizontal diffusion that is faster than the vertical diffusion (see Figure S4 for more details).

To consider the mechanisms behind the dynamics observed here, the potential variations around two structures were examined. Figure 6 shows STM images obtained at locations including steps (Figure 6a) and a vacancy (Figure 6b) and the I−V curves[22] measured at different points in the images (Figures 6c and 6d, respectively). The spatial variations of the HOMO level (E_H) and LUMO level (E_L) around the two structures were estimated from the rising parts of the I−V curves and are plotted in Figures 6e and 6f, respectively. First, for the step structure shown in Figure 6a, the apparent energy gap between the HOMO and the LUMO ($E_{HL} = |E_H - E_L|$) gradually decreases from an upper step edge (0) to the down step edge of the neighboring upper layer (4), widens at the upper step edge (5), and then the same change occurs toward the down step edge of the next upper layer. These results show that the band-structure change at the step edge is not a simple dipole-like one across the step,[23] and other mechanisms are considered to be involved. At the upper step edge, C_{60} has a smaller number of neighboring molecules than C_{60} at the terrace. Therefore, at the upper step edge, the broadening of the molecular state owing to their overlaps with neighboring molecules becomes less effective. Also, the screening of mobile carriers is weakened, that is, the value of the Hubbard on-site energy increases.[24] Both phenomena increase the HOMO−
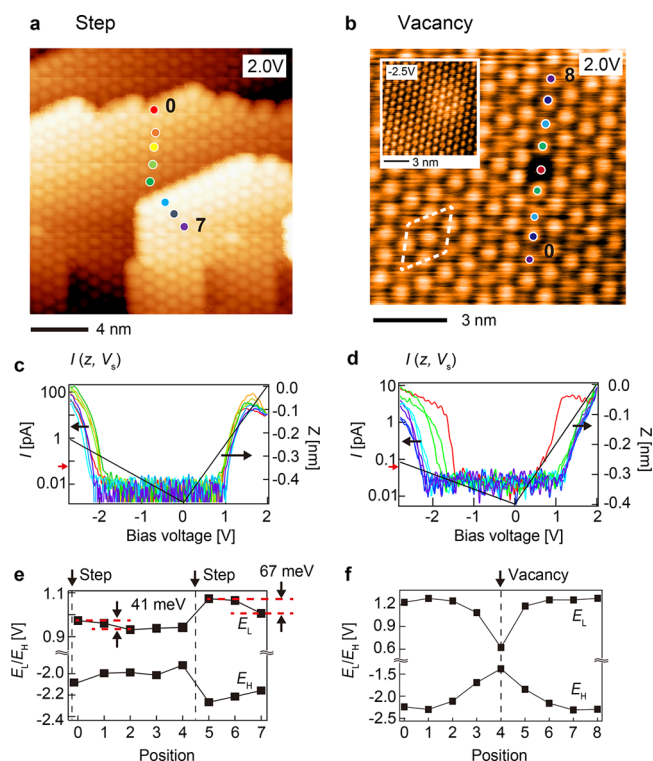
Figure 6. Analysis of the band structures of steps, a vacancy defect, and a bright defect. (a,b) STM images obtained over steps and a vacancy defect, respectively (2.0 V, 20 pA for c and 2.0 V, 10 pA for others). The inset of (b) is an STM image obtained for a negative bias voltage (−2.5 V, 10 pA). A 2×2 unit cell is drawn in (b). (c,d) $I-V$ curves obtained above the points shown in (a) and (b), respectively. Here, variable-pacing STS[24] was used to measure the energy level distribution with high accuracy. The black line in each graph shows the change in the tip−sample distance during the $I-V$ curve measurement. (e,f) E_H and E_L obtained from the rising parts of the $I-V$ curves shown in (c) and (d), respectively. When the number of layers increases, larger E_H and E_L are observed owing to TIBB; thus, the actual change may be smaller.

LUMO gap at the upper step edge. In addition, E_{HL} increases with increasing number of layers because the voltage drop in the C_{60} layer owing to TIBB increases with increasing number of layers. The observed gradual change might have been caused by the slight relaxation of the lattice near the step edge. This variation is considered to have a strong effect on electron motion in materials, as clearly shown in Figures 5c and 5d (see Figure S3 for a larger-area image). For the vacancy (Figures 6b, 6d, and 6f), E_{HL} apparently decreased owing to the formation of an in-gap state, the effect of which was observed over a distance of two molecules from the defect.

Figure 7 shows 2D snapshots measured around another defect. In the bottom topographic STM image in Figure 7(a), the C_{60} molecule indicated by the white arrow appears slightly brighter than the other molecules and is considered to have a different molecular angle from those the other equivalent C_{60} molecules in the (2×2) lattice.[25] As shown in the snapshot images in Figure 7(a), electrons were trapped only in the single bright C_{60} at 53 ps, clearly indicating that the molecule acts as a trap site for electrons. The rapid decrease in electron density in the bottom left area is considered to have been caused by the step existing in the area. Similar to the case shown in Figure 6, we carried out $I-V$ measurement around the bright defect (Figure 7b), and the results are shown in Figures 7c and

7d. For the bright molecule, E_{HL} similarly decreased owing to the formation of a shallow defect state,[25] but the change occurred within the range of a single molecule.

Finally, we review and discuss the time-resolved THz-STM data in detail. Figure 8 shows a schematic illustration of the ultrafast electron motion in the C_{60} multilayer sample. After electron injection, electrons at the upper step edge move toward the down step edge owing to the higher E_L at the upper step edge, as shown in Figure 6e. At the same time, some electrons are trapped into defect-induced gap states.

As mentioned above, the effect of V_{DC} slows down the relaxation of electrons to the Au substrate. Even under such conditions, the relaxation of electrons at the upper step edge was very fast (several ps), so it is considered that the electrons at the upper step edge move to the terrace, the lower step edge, and so forth, before relaxing to the Au substrate. An increase in electron density was observed on the terrace in the first 1 ps, suggesting carrier accumulation due to horizontal diffusion. These results correspond well to the spatial changes in band structure. Since the horizontal diffusion was fast and the distribution of injected electrons was already formed at $t_d = 1$ ps, the initial horizontal change in the red area with high electron density is not very clear in the snapshots. Finer adjustment of conditions, such as electronic excitation density and electron extraction is necessary, and we would like to make this a future work. However, a gradual decrease in the high-density area can be seen in the images in Figures 5 and 7, showing the existence of the horizontal diffusion that is faster than the vertical diffusion, as described above (see Figure S4 for more details).

As shown in Figure 5, although the spectrum changed slightly with the location, single exponential decay was observed in the spectra obtained from the top layer. The decay was fastest at step edges (C) and (D), where E_L was high, as shown in Figure 6e. It is also noted that the lifetime was long at point (A) owing to the influence of the vacancy defect indicated by the arrow. Regarding the change in the second layer from the top, an increase in electron density was observed, except at (D), on a short time scale of sub-ps to ps (τ_r) and is considered to be caused by the redistribution of electrons to smooth the in-plane potential. Then decay (τ_d) occurred on the same time scale, as was observed for the top layer. It can be seen that the lifetime was slightly longer at (E), (F), and (G) below the step (down step edge) on the second layer and that the accumulation of electrons occurred around the down step edges in both the second and third layers. The injected electrons were trapped at the down step edges and defects, and they eventually diffused to the Au(111) surface and returned to their original state.

From Figure 6e, the change in the potential at the step edge is about 40−70 meV for a distance of 2 nm, which gives us a rough estimate of about 20−35 mV/nm for the electric field. On the other hand, from spectra (C) and (D) in Figure 4b, the time required for electrons to spread away from the step edge is about 4−5 ps. By assuming these values, the mobility is roughly estimated to be 0.2−0.5 cm^2/(V s), which is higher than the macroscopically obtained value (below 0.1 cm^2/(V s) at 100 K[26,27]). This discrepancy could be due to our measurements being carried out in a local region without any structural disorder. Taking into account the temperature dependence and the electric field dependence allows a more detailed consideration, but this is not carried out here. For both the vacancy and the bright defect, electrons were
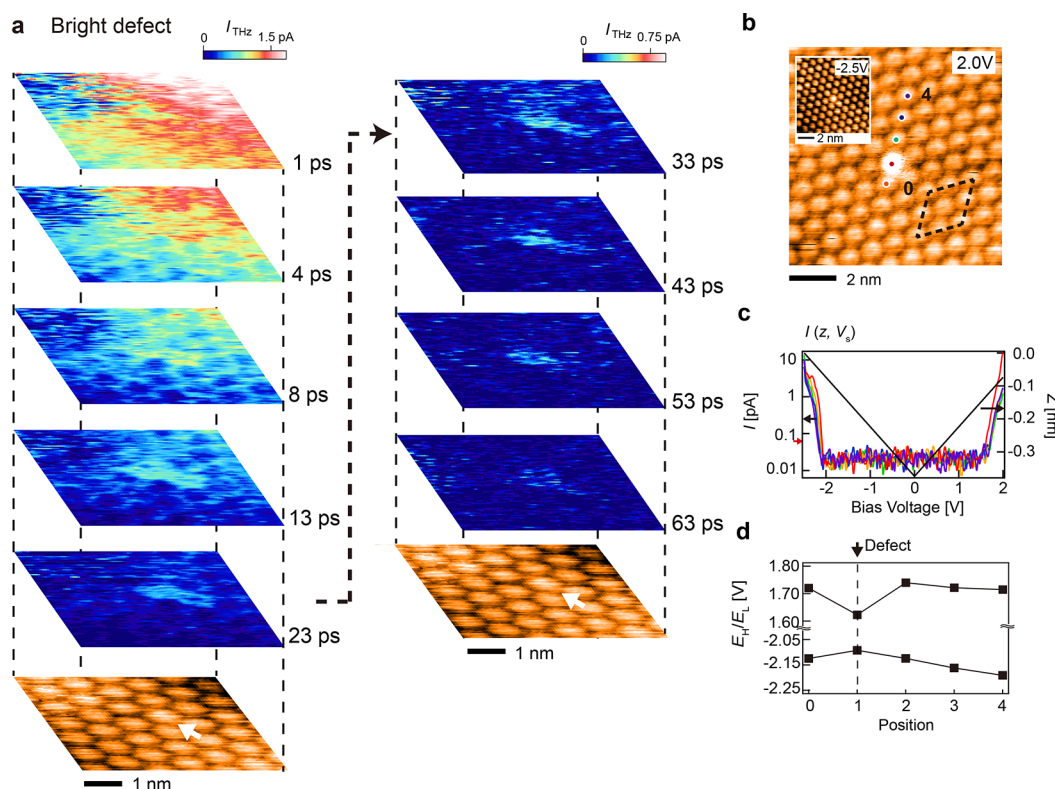
Figure 7. Time-resolved analysis of electron motion for a bright defect. (a) STM image and snapshots obtained over an area including the bright defect indicated by the white arrow. (b) STM image of the same bright defect (2.0 V, 20 pA). The inset is an STM image obtained with a negative bias voltage (−2.5 V, 10 pA). (c) I−V curves (variable-pacing STS) obtained above the points shown in (b). The black line in the graph shows the change in the tip−sample distance during the I−V curve measurement. (d) E_H and E_L obtained from the rising points of the I−V curves shown in (c).
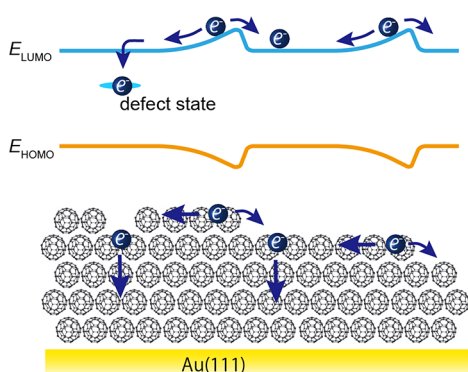
Figure 8. Model for the observed electron motion. Schematic illustration showing the ultrafast electron motion in the C_{60} multilayer sample influenced by the local modulation of the band structure and the in-gap state around surface steps and defects.

observed to be trapped for a long time. The spread sizes of electrons in the vacancy and the bright defects were ∼2 and 1 nm, as indicated by the arrows in the snapshots shown in Figures 5c and 7a, respectively. The results were in good agreement with the spread of the electronic states owing to defects shown in Figures 6f and 7b, respectively.

In conclusion, we used THz-STM to probe the ultrafast dynamics of free electrons optically excited into the LUMO of a C_{60} multilayer formed on a Au substrate. I_{THz} was utilized to probe the change in the population of free electrons under the STM tip with sub-ps time resolution. By assembling I_{THz} images taken at different delay times using the pump−probe

technique, we made a movie that shows the ultrafast movement of free electrons with nanoscale spatial resolution. Significant influences of atomic-scale surface structures with modulated local potentials on the nanoscale electron dynamics in the organic thin film were clearly demonstrated.

This method is expected to play an important role in the precise evaluation of local electronic structures and dynamics to develop new functional materials and device elements.

■ MATERIALS AND METHODS

THz-STM System. A coherent Monaco femtosecond laser (1035 nm, 40 W, 309 fs, 1−50 MHz) was used as a light source, and most of the output (39 W) was used for THz pulse generation with a $LiNbO_3$ crystal.[28] Here, high-repetition-rate and high-intensity THz pulses were generated to realize measurement with an improved S/N ratio. A repetition frequency of 16.7 (50/3) MHz (the maximum for our present setup) and a peak electric field of 250 V/cm were used, which was a sufficient electric field for driving the tunnel current. By assuming the tip−sample distance to be 1 nm and calculating the ratio of the peak voltages shown in Figures 1b and 1c, the tip enhancement factor was estimated to be 60 000, which is similar to a previously reported value.[6,29]

Sample Preparation. A C_{60} multilayer film was formed by vacuum deposition at room temperature using a clean Au(111) surface as a substrate. The average film thickness was four monolayers (MLs). A close-packed C_{60} multilayer structure was grown. Up to the third layer from the substrate, the electronic structure exhibited coupling with the Au substrate, but from the fourth layer, it had an electronic state peculiar to a

C_{60} molecule disconnected from the substrate, as reported in a previous paper.[30]

The lowest unoccupied molecular orbital (LUMO) of the first layer C_{60} was located about 0.9 eV higher than the Fermi level of the Au(111), and the highest occupied molecular orbital (HOMO)−LUMO gap of C_{60} was about 3.1 eV.[20] On the other hand, the energy of the photons of the IR pulse used was 1.2 eV. Therefore, no carrier (electron−hole pair) generation occurred inside C_{60}. To detect the weak THz current superimposed on the DC tunnel current, the THz pulse train was chopped at 415 Hz and the difference signal was detected by a lock-in amplifier. The entire experiment was performed in a vacuum (1×10^{-7} Pa) at ∼100 K using a liquid nitrogen cryostat.

Two-Dimensional Imaging. Measurements were carried out 100 times at a rate of 1.3 s/scan over 200×100 points, resulting in a total measurement time of 2 min to obtain an image. Although some fluctuation in each measurement was inevitable, the same process was expected to be repeatable, and snapshots of the dynamics were satisfactorily obtained.

■ ASSOCIATED CONTENT

Ⓢ Supporting Information

The Supporting Information is available free of charge at https://pubs.acs.org/doi/10.1021/acsphotonics.0c01572.

> Schematic illustration of electric field strength control system; Method for measuring THz near-field waveform using photoemission; Derivation of THz voltage in tunnel region; Time-resolved images of electron motion obtained over a large area (PDF)
>
> Movie S1: Movie showing the motion of electrons obtained over a large area (MP4)

■ AUTHOR INFORMATION

Corresponding Author

Hidemi Shigekawa − *Faculty of Pure and Applied Sciences, University of Tsukuba, Tsukuba 305-8573, Japan;* ⊙ orcid.org/0000-0001-9550-5148; Email: hidemi@ims.tsukuba.ac.jp

Authors

Shoji Yoshida − *Faculty of Pure and Applied Sciences, University of Tsukuba, Tsukuba 305-8573, Japan*

Yusuke Arashida − *Faculty of Pure and Applied Sciences, University of Tsukuba, Tsukuba 305-8573, Japan*

Hideki Hirori − *Institute for Chemical Research, Kyoto University, Kyoto 611-0011, Japan*

Takehiro Tachizaki − *Department of Optical and Imaging Science and Technology, Tokai University, Hiratsuka-shi, Kanagawa 259-1292, Japan*

Atsushi Taninaka − *Faculty of Pure and Applied Sciences, University of Tsukuba, Tsukuba 305-8573, Japan*

Hiroki Ueno − *Faculty of Pure and Applied Sciences, University of Tsukuba, Tsukuba 305-8573, Japan*

Osamu Takeuchi − *Faculty of Pure and Applied Sciences, University of Tsukuba, Tsukuba 305-8573, Japan*

Complete contact information is available at:
https://pubs.acs.org/10.1021/acsphotonics.0c01572

Author Contributions

S.Y., Y.A., H.H., and T.T. contributed to advance the THz-STM system. S.Y. performed experiments with H.U.; Y.A., A.T. and O.T. provided technical advice. H.S. organized and supervised the project and edited the paper with S.Y.

Notes

The authors declare no competing financial interest.

■ ACKNOWLEDGMENTS

■ REFERENCES

(1) Doherty, T. A. S.; Winchester, A. J.; Macpherson, S.; Johnstone, D. N.; Pareek, V.; Tennyson, E. M.; Kosar, S.; Kosasih, F. U.; Anaya, M.; Abdi-Jalebi, M.; Andaji-Garmaroudi, Z.; Wong, E. L.; Madéo, J.; Chiang, Y. H.; Park, J. S.; Jung, Y. K.; Petoukhoff, C. E.; Divitini, G.; Man, M. K. L.; Ducati, C.; Walsh, A.; Midgley, P. A.; Dani, K. M.; Stranks, S. D. Performance-Limiting Nanoscale Trap Clusters at Grain Junctions in Halide Perovskites. *Nature* **2020**, *580*, 360−366.

(2) Kwok, Y.; Chen, G.; Mukamel, S. STM Imaging of Electron Migration in Real Space and Time: A Simulation Study. *Nano Lett.* **2019**, *19*, 7006−7012.

(3) Terada, Y.; Yoshida, S.; Takeuchi, O.; Shigekawa, H. Real-Space Imaging of Transient Carrier Dynamics by Nanoscale Pumpg-Probe Microscopy. *Nat. Photonics* **2010**, *4*, 869−874.

(4) Yoshida, S.; Aizawa, Y.; Wang, Z. H.; Oshima, R.; Mera, Y.; Matsuyama, E.; Oigawa, H.; Takeuchi, O.; Shigekawa, H. Probing Ultrafast Spin Dynamics with Optical Pump-Probe Scanning Tunnelling Microscopy. *Nat. Nanotechnol.* **2014**, *9*, 588−593.

(5) Yoshida, S.; Yokota, M.; Takeuchi, O.; Oigawa, H.; Mera, Y.; Shigekawa, H. Single-Atomic-Level Probe of Transient Carrier Dynamics by Laser-Combined Scanning Tunneling Microscopy. *Appl. Phys. Express* **2013**, *6*, No. 032401.

(6) Cocker, T. L.; Jelic, V.; Gupta, M.; Molesky, S. J.; Burgess, J. A. J.; Reyes, G. D. L.; Titova, L. V.; Tsui, Y. Y.; Freeman, M. R.; Hegmann, F. A. An Ultrafast Terahertz Scanning Tunnelling Microscope. *Nat. Photonics* **2013**, *7*, 620−625.

(7) Cocker, T. L.; Peller, D.; Yu, P.; Repp, J.; Huber, R. Tracking the Ultrafast Motion of a Single Molecule by Femtosecond Orbital Imaging. *Nature* **2016**, *539*, 263−267.

(8) Yoshida, S.; Hirori, H.; Tachizaki, T.; Yoshioka, K.; Arashida, Y.; Wang, Z. H.; Sanari, Y.; Takeuchi, O.; Kanemitsu, Y.; Shigekawa, H. Subcycle Transient Scanning Tunneling Spectroscopy with Visualization of Enhanced Terahertz Near Field. *ACS Photonics* **2019**, *6*, 1356−1364.

(9) Shibuta, M.; Yamamoto, K.; Ohta, T.; Nakaya, M.; Eguchi, T.; Nakajima, A. Direct Observation of Photocarrier Electron Dynamics in C_{60} Films on Graphite by Time-Resolved Two-Photon Photoemission. *Sci. Rep.* **2016**, *6*, 35853.

(10) Dutton, G.; Quinn, D. P.; Lindstrom, C. D.; Zhu, X. Y. Exciton Dynamics at Molecule-Metal Interfaces: C_{60}/Au(111). *Phys. Rev. B: Condens. Matter Mater. Phys.* **2005**, *72*, No. 045441.

(11) Rosławska, A.; Merino, P.; Große, C.; Leon, C. C.; Gunnarsson, O.; Etzkorn, M.; Kuhnke, K.; Kern, K. Single Charge and Exciton Dynamics Probed by Molecular-Scale-Induced Electroluminescence. *Nano Lett.* **2018**, *18*, 4001−4007.

(12) Yoshioka, K.; Katayama, I.; Arashida, Y.; Ban, A.; Kawada, Y.; Konishi, K.; Takahashi, H.; Takeda, J. Tailoring Single-Cycle Near Field in a Tunnel Junction with Carrier-Envelope Phase-Controlled Terahertz Electric Fields. *Nano Lett.* **2018**, *18*, 5198−5204.

(13) Kawata, Y.; Yasuda, T.; Takahashi, H. Carrier Envelope Phase Shifter for Broadband Terahertz Pulses. *Opt. Lett.* **2016**, *41*, 986−989.

(14) Kronik, L.; Shapira, Y. Surface Photovoltage Phenomena: Theory, Experiment, and Applications Leeor. *Surf. Sci. Rep.* **1999**, *37*, 1−206.

(15) Yoshida, S.; Kanitani, Y.; Oshima, R.; Okada, Y.; Takeuchi, O.; Shigekawa, H. Microscopic Basis for the Mechanism of Carrier Dynamics in an Operating P-n Junction Examined by Using Light-

Modulated Scanning Tunneling Spectroscopy. *Phys. Rev. Lett.* **2007**, *98*, No. 026802.

(16) Herink, G.; Wimmer, L.; Ropers, C. Field Emission at Terahertz Frequencies: AC-Tunneling and Ultrafast Carrier Dynamics. *New J. Phys.* **2014**, *16*, 123005.

(17) Yoshioka, K.; Igarashi, I.; Yoshida, S.; Arashida, Y.; Katayama, I.; Takeda, J.; Shigekawa, H. Subcycle Mid-Infrared Coherent Transients at 4 MHz Repetition Rate Applicable to Light-Wave-Driven Scanning Tunneling Microscopy. *Opt. Lett.* **2019**, *44*, 5350.

(18) Müller, M.; Martín-Sabanés, N.; Kampfrath, T.; Wolf, M. Phase-Resolved Detection and Control of Ultrabroadband THz Pulses Coupled to a Scanning Tunneling Microscope Junction. *ACS Photonics* **2020**, *7*, 2046−2055.

(19) Garg, M.; Kern, K. Attosecond Coherent Manipulation of Electrons in Tunneling Microscopy. *Science* **2020**, *367*, 411−415.

(20) Ohno, T. R.; Chen, Y.; Harvey, S. E.; Kroll, G. H.; Weaver, J. H.; Haufler, R. E.; Smalley, R. E. C_{60} Bonding and Energy-Level Alignment on Metal and Semiconductor Surfaces. *Phys. Rev. B: Condens. Matter Mater. Phys.* **1991**, *44*, 13747−13755.

(21) Shibuta, M.; Yamamoto, K.; Ohta, T.; Nakaya, M.; Eguchi, T.; Nakajima, A. Direct Observation of Photocarrier Electron Dynamics in C_{60} Films on Graphite by Time-Resolved Two-Photon Photoemission. *Sci. Rep.* **2016**, *6*, 35853.

(22) Feenstra, R. Tunneling Spectroscopy of the (110) Surface of Direct-Gap III-V Semiconductor. *Phys. Rev. B: Condens. Matter Mater. Phys.* **1994**, *50*, 4561.

(23) He, T.; Wu, Y.; D'Avino, G.; Schmidt, E.; Stolte, M.; Cornil, J.; Beljonne, D.; Ruden, P. P.; Würthner, F.; Frisbie, C. D. Crystal Step Edges Can Trap Electrons on the Surfaces of N-Type Organic Semiconductors. *Nat. Commun.* **2018**, *9*, 2141.

(24) Fernández Torrente, I.; Franke, K. J.; Ignacio Pascual, J. Spectroscopy of C_{60} Single Molecules: The Role of Screening on Energy Level Alignment. *J. Phys.: Condens. Matter* **2008**, *20*, 184001.

(25) Große, C.; Gunnarsson, O.; Merino, P.; Kuhnke, K.; Kern, K. Nanoscale Imaging of Charge Carrier and Exciton Trapping at Structural Defects in Organic Semiconductors. *Nano Lett.* **2016**, *16*, 2084−2089.

(26) Ullah, M.; Fishchuk, I. I.; Kadashchuk, A.; Stadler, P.; Pivrikas, A.; Simbrunner, C.; Poroshin, V. N.; Sariciftci, N. S.; Sitter, H. Dependence of Meyer-Neldel Energy on Energetic Disorder in Organic Field Effect Transistors. *Appl. Phys. Lett.* **2010**, *96*, 213306.

(27) Fishchuk, I. I.; Kadashchuk, A. K.; Genoe, J.; Ullah, M.; Sitter, H.; Singh, T. B.; Sariciftci, N. S.; Bässler, H. Temperature Dependence of the Charge Carrier Mobility in Disordered Organic Semiconductors at Large Carrier Concentrations. *Phys. Rev. B: Condens. Matter Mater. Phys.* **2010**, *81*, No. 045202.

(28) Hirori, H.; Doi, A.; Blanchard, F.; Tanaka, K. Single-Cycle Terahertz Pulses with Amplitudes Exceeding 1 MV/cm Generated by Optical Rectification in $LiNbO_3$. *Appl. Phys. Lett.* **2011**, *98*, No. 091106.

(29) Yoshioka, K.; Katayama, I.; Minami, Y.; Kitajima, M.; Yoshida, S.; Shigekawa, H.; Takeda, J. Real-Space Coherent Manipulation of Electrons in a Single Tunnel Junction by Single-Cycle Terahertz Electric Fields. *Nat. Photonics* **2016**, *10*, 762−765.

(30) Dutton, G.; Zhu, X. Y. Unoccupied States in C_{60} Thin Films Probed by Two-Photon Photoemission. *J. Phys. Chem. B* **2002**, *106*, 5975−5981.